ADVANCED MATERIALS
www.advmat.de

Femtosecond Electron Diffraction Reveals Local Disorder and Local Anharmonicity in Thermoelectric SnSe

Jingjun Li, Yingpeng Qi, Qing Yang, Luye Yue, Changyuan Yao, Zijing Chen, Sheng Meng, Dao Xiang, and Jianming Cao*

In addition to long-range periodicity, local disorder, with local structures deviating from the average lattice structure, dominates the physical properties of phonons, electrons, and spin subsystems in crystalline functional materials. Experimentally characterizing the 3D atomic configuration of such a local disorder and correlating it with advanced functions remains challenging. Using a combination of femtosecond electron diffraction, structure factor calculations, and time-dependent density functional theory molecular dynamics simulations, the static local disorder and its local anharmonicity in thermoelectric SnSe are identified exclusively. The ultrafast structural dynamics reveal that the crystalline SnSe is composed of multiple locally correlated configurations dominated by the static off-symmetry displacements of Sn (≈0.4 Å) and such a set of locally correlated structures is termed local disorder. Moreover, the anharmonicity of this local disorder induces an ultrafast atomic displacement within 100 fs, indicating the signature of probable THz Einstein oscillators. The identified local disorder and local anharmonicity suggest a glass-like thermal transport channel, which updates the fundamental insight into the long-debated ultralow thermal conductivity of SnSe. The method of revealing the 3D local disorder and the locally correlated interactions by ultrafast structural dynamics will inspire broad interest in the construction of structure–property relationships in material science.

1. Introduction

Structure determines properties, which is a traditional paradigm in materials science. Understanding the intrinsic correlation between the structure and functional properties is at the core of materials science and engineering. The crystal structure based on long-range periodicity provides excellent convenience for describing and coherently controlling crystalline properties.[1] However, emerging functional crystalline materials, commonly known as crystalline disordered materials, are composed of abundant local structures that deviate from the long-range average structures.[2] Such a set of local structures, termed local disorder, has a profound impact on the functional properties of phonons, electrons, and spin subsystems, such as the correlated electronic states, thermal conductivities, and structural transitions.[3] In conventional crystallographic terms, there is no distinction between crystalline materials with and without local disorder because their configurational averages are characterized by the same crystallographic space group. Although considerable effort has been devoted to determining the local disorder in such crystalline-disordered materials, the quantitative 3D characterization of the local atomic configuration and local potential energy environment remains a significant challenge.[3e,h,4] It is unclear whether the local atomic configuration is random or dominated by locally correlated interactions.[5] In this study, we propose the use of femtosecond electron diffraction to detect nonequilibrium structural dynamics in

J. Li, Y. Qi, L. Yue, C. Yao, J. Cao
Center for Ultrafast Science and Technology
School of Physics and Astronomy
Shanghai Jiao Tong University
Shanghai 200240, China
E-mail: qiyp@sjtu.edu.cn

Q. Yang, S. Meng
Beijing National Laboratory for Condensed Matter Physics
and Institute of Physics
Chinese Academy of Sciences
Beijing 100190, China

Z. Chen, D. Xiang
Key Laboratory for Laser Plasmas (Ministry of Education)
School of Physics and Astronomy
Shanghai Jiao Tong University
Shanghai 200240, China

Z. Chen, D. Xiang
Collaborative Innovation Center of IFSA (CICIFSA)
Shanghai Jiao Tong University
Shanghai 200240, China

S. Meng
School of Physical Sciences
University of Chinese Academy of Sciences
Beijing 100049, China

S. Meng
Songshan Lake Materials Laboratory
Dongguan, Guangdong 523808, China

The ORCID identification number(s) for the author(s) of this article can be found under https://doi.org/10.1002/adma.202313742

DOI: 10.1002/adma.202313742

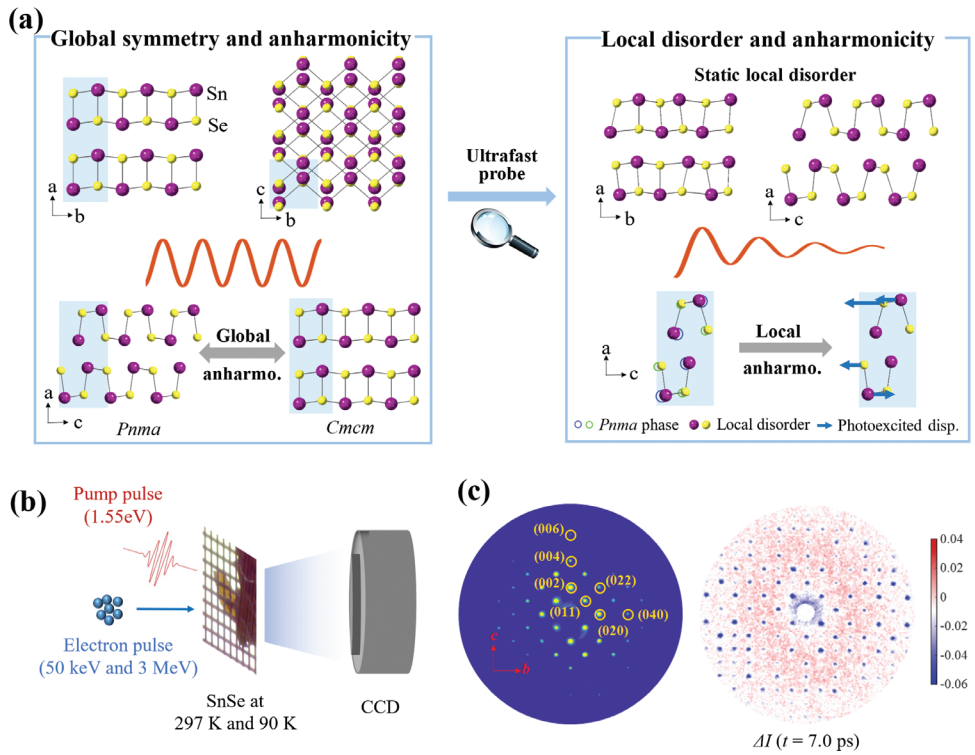

Figure 1. Probing the static local disorder and local anharmonicity in SnSe by femtosecond electron diffraction. a) Left: Crystal structure of SnSe in the *Pnma* phase with the side view (*a*–*b* and *a*–*c* plane) and the top view (*b*–*c* plane). The unit cell is labeled by light blue rectangles. The oscillation curve in the middle panel indicates a long-range coherence of the rigid crystal structure. The bottom panel displays the structural transition from the *Pnma* to *Cmcm* phase dominated by a global anharmonicity. Right: The top panel is the schematic of the static local disorder along the *b* and *c* axes with dominant off-symmetry displacements of Sn atoms among unit cells. Such local disorders reduce the long-range coherence denoted by a damped oscillation curve in the middle panel. The bottom panel displays the photoexcited displacements of the Sn and Se atoms representing the local anharmonicity. The hollow and solid circles indicate the rigid crystal and locally disordered structures respectively. b) Schematic of the ultrafast pump–probe experiments with 50 keV and 3 MeV femtosecond electron diffraction. The SnSe nanofilm on the TEM grid is pumped by 35 fs, 800 nm laser pulse at 297 and 90 K. The diffraction patterns at different time delays are recorded by a charged-coupled device camera. (c) Left: Static diffraction pattern acquired during experiments. Several Bragg reflections are labeled by the Miller index. Right: Differential pattern at 7.0 ps after photoexcitation.

crystalline-disordered materials and reveal the intrinsic local disorder and local anharmonicity with femtosecond-picometer temporospatial resolution. Considering the thermoelectric SnSe as an example, using an ultrafast laser-pump electron probe, the local disorder and local anharmonicity are explicitly disentangled from the global symmetry and global anharmonicity, as shown in **Figure** 1a. The identified local disorder with eight degenerated atomic configurations is evidence of the locally correlated interactions in crystalline-disorder materials. The local disorder and local anharmonicity indicate a glass-like thermal transport channel beyond the phonon picture in typical crystals, which updates the fundamental insight into the long-debated ultralow thermal conductivity of SnSe.

Thermoelectric materials, which enable direct conversion between thermal and electrical energy, are considered promising alternatives to meet the challenges of the global energy dilemma.[6] Single crystalline SnSe has drawn strong attention recently in the thermoelectric community due to the surprising ultralow thermal conductivity ($\kappa_{lat} < 1$ Wm^{-1} K^{-1}) and the extraordinarily high thermoelectric figure of merit ($ZT > 2$) in such a simple binary compound.[7] The underlying physical mechanisms of the ultralow thermal conductivity at both ambient and high temperatures remain controversial. The crystal structure of the layered SnSe, as shown in Figure 1a (left), holds a puckered distortion along the *c* axis and a thermal-induced structural transition from the *Pnma* to the *Cmcm* phase at ≈807 K.[7b,8] The phonon mean free path of ≈0.84 nm at room temperature in SnSe approaches lengths of interatomic distances similar to those in disordered materials.[9] Using inelastic neutron scattering measurements, the ultralow thermal conductivity can be qualitatively attributed to lattice anharmonicity across the structural transition.[8,10]

D. Xiang
Tsung-Dao Lee Institute
Shanghai Jiao Tong University
Shanghai 200240, China
D. Xiang
Zhangjiang Institute for Advanced Study
Shanghai Jiao Tong University
Shanghai 200240, China
J. Cao
Physics Department and National High Magnetic Field Laboratory
Florida State University
Tallahassee, FL 32310, USA

However, recent experiments have shown that the anharmonic behavior begins near room temperature, which is substantially lower than the structural transition temperature.[11] The relatively flat thermal conductivity without an abrupt decrease at high temperatures also challenges the structural-transition-induced lattice anharmonicity model. In addition to lattice anharmonicity, vacancies and off-stoichiometry defects in the ground state of SnSe were identified.[7d,12] Most SnSe samples used in research were intrinsically p doping, which derives from vacancy defects.[7b,12a] In typical crystals, the phonon picture is valid, therefore, the phonon anharmonicity and the scattering among phonons are used to describe the thermal transport; while in highly disordered materials, such as glassy and amorphous materials, the phonon picture is invalid and the heat is supposedly carried by random walk among uncorrelated oscillators. Recent studies suggest that the two thermal transport channels, i.e., the crystal thermal transport channel and the glass-like thermal transport channel, coexist in crystalline thermoelectric materials with ultralow thermal conductivity.[4d,13] Analogously, the point defects and associated local structures in SnSe may invalidate the phonon picture and cause a combined thermal transport with the crystal transport channel and the glass-like transport channel.

Characterizing the local structure and local disorder in crystalline materials is an experimental challenge. Conventional methods, such as the neutron total scattering, characterize the local structure of the equilibrium state.[3e,4,14] Therefore, the time-domain evolution of the local disorder, either static or dynamic, with the underlying feature of the local potential energy landscape is lost.[3h] Structural evolution in the time domain is a potentially suitable method for identifying the local structure contained in the ground state.[3f,15] Based on this perspective, we propose the use of femtosecond electron diffraction to quantify the local structure and the local disorder. The local disorder considered here is intrinsic to material systems, contrary to photoinduced disorder and defects.[16] A schematic illustration of femtosecond electron diffraction is shown in Figure 1b. By varying the time delay between the pump laser and probe electron, the transient structural dynamics were detected with a picometer spatial resolution and temporal resolution of up to ≈50 fs.[17] The acquired prototypical diffraction and the differential patterns are shown in Figure 1c. Generally, the local structure is distinct from the average lattice structure, causing anomalous intensity changes in both Bragg reflections and diffuse scattering.[18] The Bragg reflections have a greater intensity than diffuse scattering by several orders of magnitude; therefore, they has a higher signal-to-noise ratio and higher priority in quantifying the local structure.[3f,15,19] The local structure has a limited correlation length over one to a few unit cells, and the Bragg reflection intensity is determined by such a supercell.[16a,20] The parameters associated with the local structure, such as the thermal vibration, static local disorder, and photoexcited displacement, can be identified by the ultrafast structural dynamics with the structure factor calculation (refer to the Experimental Section). We confirm this methodology by the transient structural dynamics of SnSe: in the picosecond time scale, the comprehensive study of all acquired Bragg reflections exclusively identifies the static local disorder with multiple atomic configurations; in the femtosecond time scale, the ultrafast photoexcited displacement within 100 fs further bolsters the local disorder model, and indicates the anharmonicity of the local disorder.

2. Identification of the Local Disorder in the *Pnma* Phase of SnSe

SnSe nanofilms with thicknesses of ≈50 nm were exfoliated from the bulk crystal and carefully characterized, as shown in Section S1 in the Supporting Information. With 800 nm femtosecond laser excitation, the threshold fluence, photoexcited carrier density, and photoinduced temperature rise are summarized in Section S2 in the Supporting Information. The crystallographic *b* axis is the high-symmetry axis and thus the intensity changes of the Bragg reflections (0*k*0) (k = 2, 4, 6) along this axis were analyzed first. In **Figure 2**a, the intensities of the three reflections decayed simultaneously with almost the same amplitude (≈1:1:1) after photoexcitation. The temporal evolution was well-fitted by a single exponential function with a time constant of ≈3.9 ps, indicating a single physical process. Photoexcitation-enhanced thermal vibration (the Debye-Waller effect) is expected to dominate this behavior.[15,21] The calculated intensity changes of the three reflections follow the s^2 dependence ($-\ln(I/I_0) = a{\cdot}s^2$, s is the scattering vector and a is constant) with the ratio of ≈1:4:9, that is, significantly larger intensity changes of the higher order reflections than that of the lower order reflections, as shown in the inset of Figure 2a and Section S3.1 in the Supporting Information. Therefore, the Debye-Waller effect could not reproduce the experimental phenomenon. We excluded the possible effects of the inhomogeneous laser pump, tilt of the sample, and multiple scattering effect (refer to Sections S3.2,S3.3, Supporting Information).[22] Other possible contributions from arbitrary atomic displacements, photoinduced formation of polarons, stacking faults, and photoinduced changes of the atomic form factor were also excluded by comprehensive studies (refer to Section S3.4–S3.7, Supporting Information).[16a,20,23] Consequently, except for the above analyses based on the rigid crystal structure of the *Pnma* phase, the probable static local off-symmetry displacements (i.e., static local disorder) induced by vacancies must be introduced in the ground state of SnSe.[12a–c]

Before quantifying the static local disorder, we first identified the structural dynamics after photoexcitation. The pump-fluence-dependent intensity change of the (020) reflection is shown in Figure 2b. At varying time delays, the inset of Figure 2b shows a linear increase of the intensity change as a function of the pump fluence, following the conventional character of the Debye-Waller effect. Closing to the threshold fluence of ≈9.5 mJ cm^{-2}, the intensity change of the (020) (and (040)) reflection is better fitted by a biexponential function with the time constants of $\tau_1 = 3.9 \pm 0.7$ ps (3.1 ± 0.7 ps) and $\tau_2 = 28.4 \pm 6.8$ ps (63.3 ± 45.0 ps), as shown in Figure 2c. Such a two-step intensity change suggests a fast electron–phonon coupling and a subsequent slow phonon–phonon coupling.[24] In the inset of Figure 2c, the amplitudes of the biexponential fit (a_1 and a_2) for the (020) reflection are equal to those of the (040) reflection, which indicates that the time-domain separated electron–phonon and phonon–phonon coupling cause the same comparable intensity changes between the (020) and (040) reflections. Therefore, the photoinduced Debye-Waller effect in the ground state of SnSe with a static local disorder dominates the intensity change over the entire time scale.

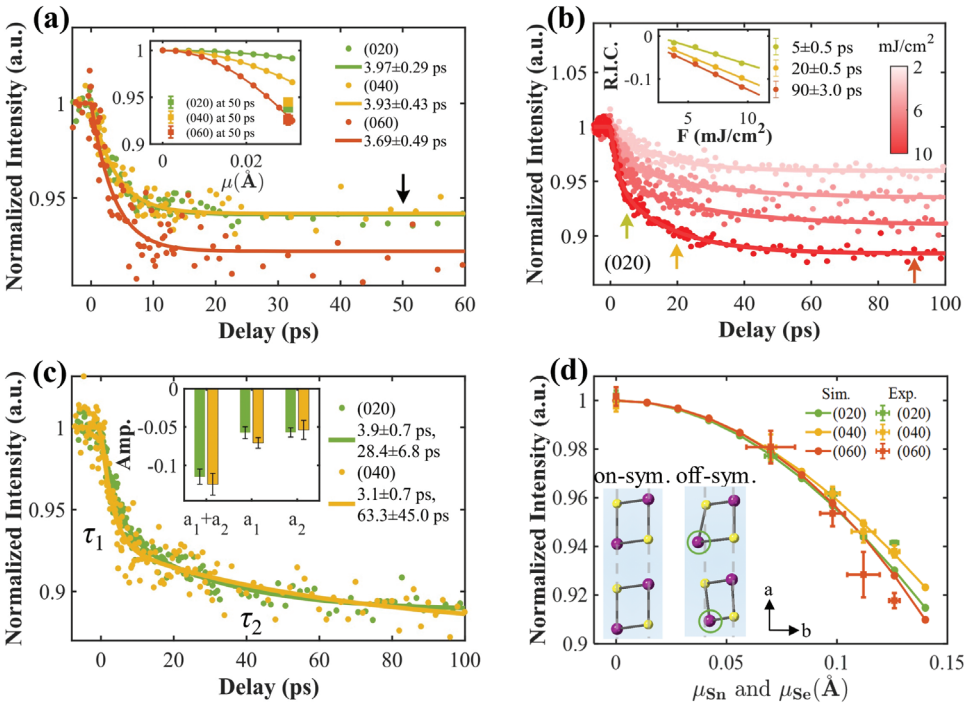

Figure 2. Identification of the static local disorder projected on the crystallographic *b* axis ((0*k*0), $k = 2, 4, 6$) in the *Pnma* phase of SnSe. a) Intensity changes of Bragg reflections (0*k*0) as a function of the time delay with the pump fluence of 7.3 mJ cm^{-2}. The solid lines represent the fit with a single exponential function. In the inset, the dotted lines are calculated intensity changes as a function of the thermal vibration amplitude and the solid squares with error bars are experimental intensity changes at the delay time of 50 ps as marked by the black arrow. b) Temporal evolution of the intensity of the (020) reflection at different pump fluences. The inset is, as a function of the pump fluences, the relative intensity change (R.I.C.) at the time delay of 5, 20, and 90 ps as marked by arrows in the main panel and the solid lines represent the linear fit. c) Intensity decay of the (020) and (040) reflection at the pump fluence of 9.5 mJ cm^{-2}, with a biexponential fit (τ_1 and τ_2). The amplitudes of the fit (a_1 and a_2) are compared in the inset. d) Experimental and calculated intensity changes with locally disordered structures as a function of the thermal vibration amplitude (μ_{Sn} and μ_{Se}). The solid squares are experimental intensities at the time delay of -1 ± 1, 2 ± 0.5, 5 ± 0.5, 10 ± 1.0, and 30 ± 5.0 ps. The horizontal error bars represent the calculated thermal vibration corresponding to the experimental intensity change (the vertical error bars). The inset displays the structure of the local disorder (off-sym.) used in the calculation and the rigid crystal structure (on-sym.). The dominant off-symmetry Sn atoms are represented by green circles. The gray dashed lines represent the position of the fraction coordinates 1/4 and 3/4.

The intensity changes of the other reflections in Section S4 in the Supporting Information further confirm these structural dynamics.

To quantify the static local disorder and Debye-Waller effect, we searched for the best fit between the experimental and calculated intensity changes over the (0*k*0) reflections along the *b* axis (refer to details in Section S3.8, Supporting Information). The random substitution of Sn with vacancies induces potentially random local distortions within unit cells. The diffuse scattering in Sections S1,S9 in the Supporting Information shows no supercells signature; therefore, the correlation length of the local disorder is within a single unit cell. The unit cell of SnSe in the *Pnma* phase contains eight atoms. Eight static displacements for each atom ($\Delta\gamma_{1\_disp}$ to $\Delta\gamma_{8\_disp}$) and two thermal vibrations (μ_{Sn} and μ_{Se}) are used in searching for the best fit to experimental results at 60 ps. For further refinement, a monotonous increase of μ_{Sn} and μ_{Se} is used to mimic the experimental Debye-Waller effect in the time domain. In addition to the (0*k*0) reflections along the *b* axis, the reflections along the *c* axis and diagonal direction were involved in searching for the overall best fit to the intensity changes of all experimentally observed Bragg reflections. In this way, eight local structures with dominant static off-symmetry displacements of Sn and thermal vibration amplitudes were ascertained (refer to Table S5.1,S5.2, Supporting Information). Considering the first local structure in Table S5.1 in the Supporting Information as the ground state, Figure 2d shows excellent agreement between the experimental and calculated intensity changes of the (0*k*0) reflections as a function of the thermal vibration amplitude. The time-domain evolutions of the experimental and calculated intensity changes in Figure S6 in the Supporting Information also show good agreement. The inset of Figure 2d shows the contrast between the rigid unit cell and locally disordered structure used in the calculation. The main characteristic of this locally disordered structure is that the two Sn atoms marked by green circles move away from the high-symmetry position (gray dashed lines) in opposite directions. Because the average crystalline structure is the *Pnma* phase without any anomalous in the static diffraction pattern, we term the identified multiple local structures with static off-symmetry displacements as a static local disorder.

In addition to the static local disorder along the *b* axis, the following study indicates that the crystal structure projected onto the *c* axis displays local disorder. **Figure 3a** shows the time-resolved intensity change of the (00*l*) ($l = 2, 4, 6$)

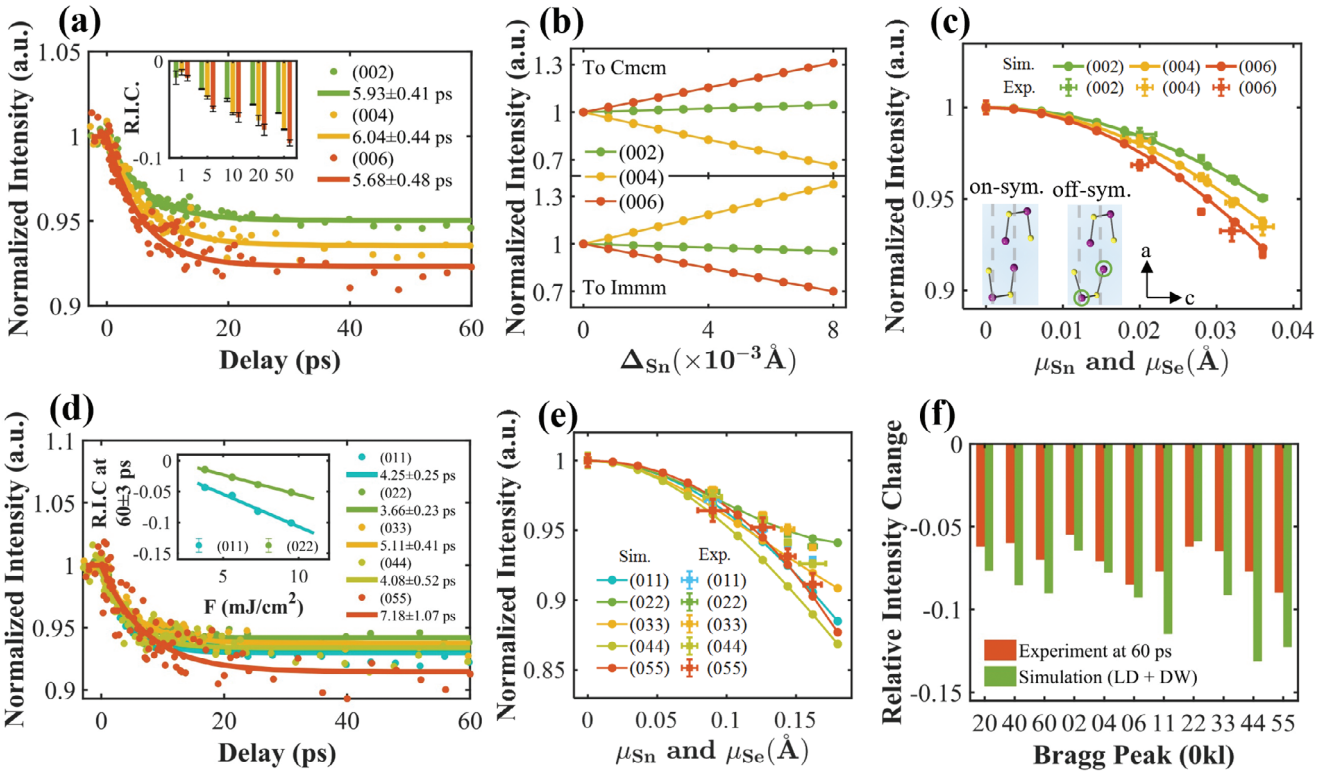

Figure 3. Identification of the static local disorder projected on the crystallographic *c* axis ((00*l*), l = 2, 4, 6) and diagonal axis ((0*ii*), i = 1, 2, 3, 4, 5) in the *Pnma* phase of SnSe. a) Time-resolved intensity changes of (00*l*) reflections along the *c* axis. The inset is the relative intensity change (R.I.C.) at different time delays (ps). b) Calculated intensity changes with the phase transition to the *Cmcm* phase or *Immm* phase. c) Experimental and calculated intensity changes with locally disordered crystal structures as a function of the thermal vibration amplitude (μ_{Sn} and μ_{Se}). The solid squares represent the experimental intensity changes at the time delay of −1 ± 1, 2 ± 0.5, 5 ± 0.5, 10 ± 1.0, and 30 ± 5.0 ps. The horizontal error bars represent the calculated thermal vibration corresponding to the experimental intensity change (the vertical error bars). The inset displays the structure of the local disorder (off-sym.) used in the calculation, and the rigid crystal structure (on-sym.). The dominant off-symmetry Sn atoms are labeled by green circles. The gray dashed lines represent the position of Sn atoms in the rigid *Pnma* phase. d) Intensity changes of (0*ii*) reflections along the diagonal axis as a function of the time delay. The inset displays R.I.C. of the (011) and (022) reflection at 60 ps with increasing pump fluence and solid lines are the linear fit. e) Experimental and calculated intensity changes of (0*ii*) reflections with locally disordered crystal structures as a function of the thermal vibration amplitude (μ_{Sn} and μ_{Se}). The solid squares represent the experimental intensity changes at −1 ± 1, 2 ± 0.5, 5 ± 0.5, 10 ± 1.0, and 30 ± 5.0 ps. f) Bar chart showing the experimental intensity change at 60 ps and the simulated intensity change with the local disorder (LD) and the Debye-Waller effect (DW).

reflections along the *c* axis. The exponential intensity decay with a time constant of ≈5.9 ps suggests a single physical process after photoexcitation. The relative intensity changes of the three reflections at different time delays are summarized in the inset of Figure 3a. The amplitudes of these intensity changes increased monotonically as a function of the time delay, suggesting a consistent physical process over the three reflections.

In contrast to the highly symmetric crystal structure along the *b* axis, the *c* axis contains a puckered structural distortion in the *Pnma* phase of SnSe, as shown in Figure 1a. At temperatures above 807 K, the structural transition from the *Pnma* to *Cmcm* phase causes significant atomic displacements along the *c* axis.[7b,8,10] Therefore, a possible photoinduced structural transition needs to be evaluated.[25] Figure 3b shows the calculated intensity change of the (00*l*) reflections with the structural transition to the *Cmcm* and *Immm* phases.[25a] Neither structural transition reproduced the experimental intensity changes. The calculated temperature increase of 234 K after photoexcitation is far below the temperature required for the transition to the *Cmcm* phase (refer to Section S2, Supporting Information). Therefore, photoinduced structural transition to high-symmetry phases can be excluded. Similar to the analysis of the *b* axis, we excluded other possible mechanisms that may dominate the time-resolved intensity changes along the *c* axis in the rigid *Pnma* phase (refer to Sections S5.1,S5.2, Supporting Information). Consequently, static local disorder along the *c* axis must be introduced into the *Pnma* phase. The consistent physical process, based on the exponential intensity decay in Figure 3a and the pump fluence dependence in Section S5.3 in the Supporting Information, is, therefore, a Debye-Waller effect. By structural factor calculation, the global fit of the intensity changes over all experimentally observed Bragg reflections along the *b* axis, *c* axis, and diagonal direction confirmed the Debye-Waller effect and eight local structures, as shown in Tables S5.1,S5.2 in the Supporting Information. With the first local structure in Table S5.2 in the Supporting Information, the calculated intensity change of the (00*l*) reflection as a function of thermal vibration

amplitude (μ_{Sn} and μ_{Se}) displays an excellent agreement with the experimental results, as depicted in Figure 3c. The time-domain evolutions of the experimental and calculated intensity changes in Figure S11 in the Supporting Information also show good agreement. The inset of Figure 3c displays the contrast between the rigid unit cell and locally disordered structure used in the calculation. The main characteristic of this locally disordered structure is that the two Sn atoms marked by green circles move away from the high-symmetry positions (gray dashed lines).

Reflections (0*ii*) (i = 1, 2, 3, 4, 5) along the diagonal direction play a role in connecting the reflections between the two orthogonal *b* and *c* axis. Searching for the best fit along the *b* and the *c* axis respectively provides two libraries containing both the locally disordered structure and thermal vibration amplitude. The time-resolved intensity change of the diagonal reflection (0*ii*) was determined using the parameters in the two libraries. The single exponential intensity decay of the (0*ii*) reflection and the linear intensity change with increasing pump fluence in Figure 3d suggest that the Debye-Waller effect dominates the physical process, in line with the *b* and *c* axis. Therefore, we calculated the intensity changes and searched for the best fit for the experimental intensity changes of the (0*ii*) reflections using the two identified libraries (refer to Section S6, Supporting Information). Considering the first local structure in Table S5.1,S5.2 in the Supporting Information as the ground state, Figure 3e displays the good agreement between the experimental and calculated intensity changes of the (0*ii*) reflection as a function of the thermal vibration amplitude. In Figure 3f, the bar chart shows excellent agreement between the experimental intensity changes of all acquired Bragg reflections at 60 ps and the calculated intensity changes with the locally disordered structure and Debye-Waller effect. At a low temperature of ≈90 K, the local disorder and Debye-Waller effect dominate the structural dynamics along the three axes are also confirmed (refer to Section S7, Supporting Information). Finally, all the above quantitative analyses of the intensity change over all acquired Bragg reflections on the picosecond time scale exclusively identified the static local disorder in the ground state of SnSe. With state-of-the-art density function theory (DFT) simulation, any single local structure in Tables S5.1,S5.2 in the Supporting Information is not stable and relaxes toward the atomic arrangement in the *Pnma* phase; therefore, the multiple local structures should be organized as a whole. Machine learning-based interatomic potential models are required to make the multiple local structures fit together and form a real material system with thousands of atoms, which is beyond the scope of this study.[26] Alternatively, we performed a simplified DFT simulation, and the local structure acquired by substitution of a single Sn position with a vacancy qualitatively agrees with the experimentally identified local disorder model (refer to Section S10, Supporting Information).

3. Identification of the Anharmonicity of the Static Local Disorder

The identified static local disorder in the *Pnma* phase of SnSe indicates an intermediate state between the crystal and glassy phase, which is a fundamental characteristic of crystalline disordered materials.[2] Such locally disordered structures induced by point defects generally cause localized vibrational modes.[27] In **Figure 4a**, the intensity of the (015) reflection increased rapidly with a time constant of ≈50 fs and an amplitude of ≈7% (refer to details in Movie S1, Supporting Information), whereas the intensity of the (013) and (011) reflections remained unchanged in this ultrafast time scale. Any thermal vibrations or atomic displacements in the rigid *Pnma* phase cannot cause such femtosecond intensity changes (refer to Section S8.1, Supporting Information). Therefore, local structures distinct from the *Pnma* phase must be introduced into the ground state, which coincides with the local disorder model determined by picosecond structural dynamics described in the previous section. Based on this consistent physical picture, we considered the identified local disorder as the ground state and searched for the best fit between the calculated and experimental intensity change within 0.3 ps over the (013), (015) and (00*l*) (l = 2, 4, 6) reflections. The calculation results indicated that the femtosecond structural dynamics were derived from the photoinduced atomic displacement (refer to Section S8.2, Supporting Information). For each static local structure shown in Table S5.2 in the Supporting Information, 13 photoinduced displacements were identified (refer to Table S6, Supporting Information). Figure 4b (left) shows a schematic of the rigid crystal structure, static local disorder (first in Table S5.2, Supporting Information), and photoinduced local displacement (first in Table S6, Supporting Information). Figure 4c displays the great agreement between the experimental and calculated intensity changes with a uniform increase in the amplitude of the photoinduced local displacement.

To further identify the femtosecond structural response, we performed time-dependent density functional theory molecular dynamics (TDDFT-MD) simulations on the rigid *Pnma* phase of SnSe. The dominant motion after ultrafast photoexcitation was the interlayer shear displacement toward the *Immm* phase, as shown in Figure 4d, which was distinct from the experimentally observed displacements. Therefore, the local disorder plays a decisive role in determining the femtosecond structural responses. The calculated displacement of ≈0.1 Å in Figure 4d is one order of magnitude larger than the maximum displacement in the previous study.[25a] This remarkable discrepancy may derive from that the local disorder enhances the energy relaxation to the Debye-Waller effect and reduces the energy flow to the structural transition. The photoinduced local displacement suggests the anharmonicity of the local structure associated with local oscillation modes (refer to discussion in Section S8.2, Supporting Information), analogous to the soft local vibrational modes in glasses.[28] The ultrafast intensity change within ≈0.1 ps in Figure 4a is generally one-quarter of the period of the oscillation modes.[29] Accordingly, the average frequency (energy) of the oscillators was 2.5 THz (10.3 meV), which is comparable to that of the Einstein oscillators in other thermoelectric systems revealed by inelastic X-ray scattering.[4d] Therefore, the ultrafast intensity change indicates the probable signature of Einstein oscillators, a thermal conduction channel beyond the phonon picture, in crystalline SnSe.[13a] These THz Einstein oscillators may lower the thermal conductivity of SnSe in two

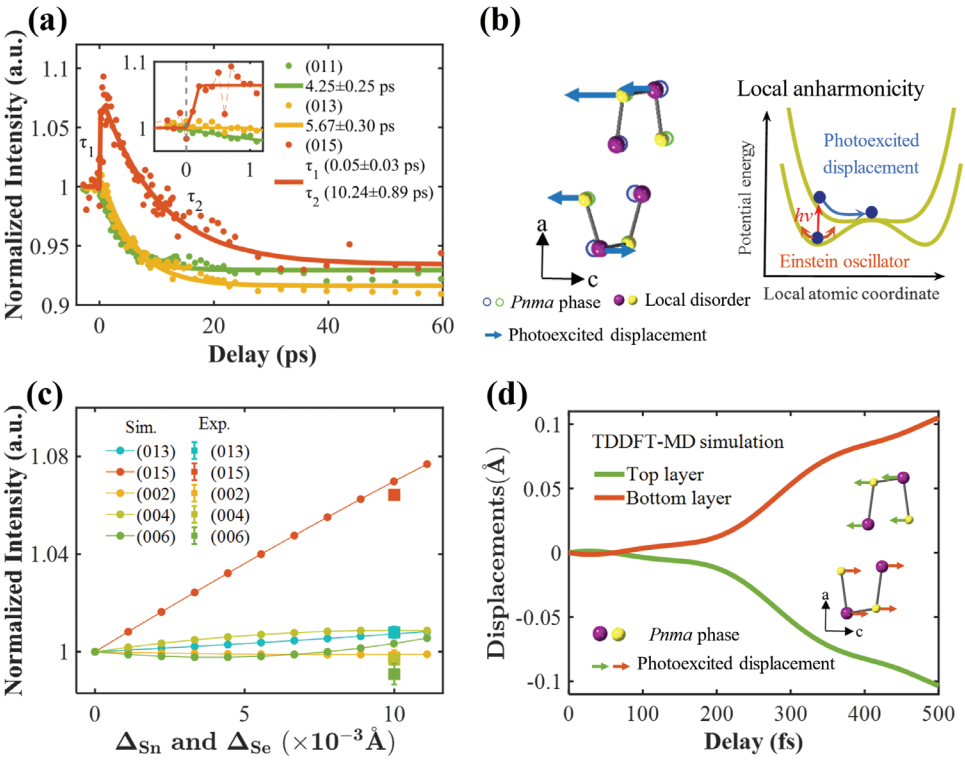

Figure 4. Identification of the anharmonicity of the local disorder. a) Anisotropic intensity changes of Bragg reflections as a function of the time delay. The inset is the temporal evolution within the first 1.2 ps. b) Left: Photoexcited atomic displacements, indicated by arrows, in the locally disordered structure. The hollow and solid circles represent the rigid crystal structure and locally disordered structure respectively. Right: Schematic illustration of the local potential energy surfaces of the Einstein oscillators and the photoexcited displacement in the locally disordered structure. c) Calculated intensity changes with increasing the displacement of Δ_{Sn} and Δ_{Se}. The locally disordered structure and the directional displacements shown in (b) are used in the calculation. The solid squares are the experimental intensity changes at 0.3 ± 0.1 ps. d) Photoexcited interlayer shear displacement in the rigid *Pnma* phase of SnSe by TDDFT-MD simulation. The inset is the schematic illustration of the interlayer shear displacements.

ways: first, the Einstein oscillators scatter the heat-carrying lattice phonons; second, the anharmonicity of the Einstein oscillators enhances the oscillator-phonon scattering with increasing temperature. Figure 4b (right) displays the schematic illustration of the local potential energy surfaces of the Einstein oscillators in the ground and excited states, and the photoexcited local displacements.

4. Discussion and Conclusion

For crystalline materials with ultralow thermal conductivity, the intermediate regime where both the crystal-like and glass-like thermal transports are associated is a hot topic in experiments and theory, but it is still under debate.[13,30] Determining the local structure is critical because understanding the ultralow thermal conductivity remains phenomenological by fitting simplified scattering models to the experimental data.[13a,30] Using a combination of femtosecond electron diffraction, structure factor calculations and TDDFT-MD simulations, we exclusively identified the static local disorder and the anharmonicity of the local disorder in thermoelectric SnSe. We attribute the local disorder with multiple atomic configurations to intrinsic vacancy defects in the SnSe sample (refer to details in Section S1,S10, Supporting Information). In contrast to the previous lattice anharmonicity across the *Pnma* to *Cmcm* transition, the quantified local disorder and local anharmonicity directly indicate a glass-like thermal transport channel.[8,10] These local structural characteristics probably also disentangle the mysterious anharmonic behavior and the unusual in-gap states at or below room temperature in SnSe.[11,31] Therefore, identifying the local structure updates the fundamental insight into the long-debated ultralow thermal conductivity in SnSe and provides the necessary structural information to further quantify the theoretical thermal transport model.[12a] To the best of our knowledge, the anharmonicity of the local disorder is revealed unprecedentedly and the microscopic picture indicates the probable THz Einstein oscillators with the energy of ≈10.3 meV.[13a] During the preparation of our paper, several studies also reported the ultrafast structural dynamics of SnSe, and some mistakes in these studies are discussed in Section S11 in the Supporting Information.[20,25]

In this study, we used femtosecond electron diffraction to reveal the local disorder and local anharmonicity in crystalline disordered materials. The global fit of the intensity changes of all acquired Bragg reflections over the entire femtosecond to picosecond time-scale enables the quantification of a consistent physical model toward the local disorder and local anharmonicity. Our method offers several advantages over conventional methods for probing local structures.[3e,h,4] First, the temporal evolution of the

local structure was detected; therefore, the static and dynamic local structures can be disentangled, which was previously difficult to achieve.[3h] Second, the anharmonicity of the local structure, determined by the locally correlated interactions among the phonon, electron and spin subsystems, can be revealed by ultrafast electronic excitation.[3a–g,15,19] Third, the 3D local structure with sub-angstrom displacement can be identified quantitatively by ultrafast structural response, and both the dimension and precision of the determined local structure are higher than that detected by conventional static total scattering and pair distribution function methods.[3e,h,4] In addition to ultrafast diffuse scattering, the ultrafast dynamics of Bragg reflections were demonstrated to identify the local structure in our study (refer to discussions in Section S11, Supporting Information).[16a,20] The 2D in plane local disorder in the present work can be simply extended to 3D by additional measuring ultrafast dynamics of the out-of-plane Bragg reflections. The local disorder and locally correlated interactions are pervasive and indispensable in a broad range of functional materials.[2,3,13a,32] The identification of the local structure lays the foundation for the theoretical and experimental study of the functional properties of the phonon, electron and spin subsystems. Therefore, we expect that the probing method and the sophisticated data analysis in our study will inspire broad interest in the fields of materials science and ultrafast science.

5. Experimental Section

keV and MeV Femtosecond Electron Diffraction: The experiments were performed on both the 50 keV and 3 MeV femtosecond electron diffraction system. For the keV femtosecond electron diffraction system, the 800 nm, 35 fs laser, and 1 kHz laser pulse (Spectrum Physics Spitfire Ace-35F) was divided into two pulses. One laser pulse used to pump was focused on the sample with a spot size of ≈500 µm full width at half maximum (FWHM) and an incidence angle around 10° off the sample's normal direction. Another laser pulse was first tripled to 266 nm, then focused on the photocathode to generate the probe electron pulse. The spot size of the electron pulse on the sample was ≈200 µm (FWHM) focused by a magnetic lens. The diffraction pattern was imaged by a phosphor screen (P43) and recorded by an electron-multiplying charge-coupled device (Andor iXon Ultra 888). The overall temporal resolution of the system was ≈500 fs. The base temperature of the sample in experiment was controlled by liquid nitrogen.

For the MeV femtosecond electron diffraction system, the 800 nm, 30 fs, and 100 Hz laser pulse (Vitara and Legend Elite Duo HE, Coherent) was split into the pump and the probe pulse. The pump pulse excited the sample and the probe pulse was frequency tripled in nonlinear crystals before illuminating a photocathode for electron pulse generation. After being accelerated by an intense radio-frequency field to relativistic velocity (≈0.989c), the electron pulse went through a double-bend achromatic lens for pulse compression and jitter removal. The spot size of the electron pulse on the sample was ≈100 µm FWHM, around five times smaller than the size of the pump laser, ensuring a homogeneous photoexcitation. The diffraction pattern was imaged by a phosphor screen (P43) and recorded by an electron-multiplying charge-coupled device (Andor iXon Ultra 888). The overall temporal resolution of the MeV femtosecond electron diffraction (FED) system was ≈50 fs. Further details for the system can be found in Ref. [17] In the experiment, the keV and MeV femtosecond electron diffraction systems gave the same time-resolved structural dynamics.

Sample Preparation and Characterization: Single crystal SnSe nanofilms were prepared via mechanical exfoliation from the bulk crystal and transferred to transmission electron microscopy (TEM) grids for femtosecond electron diffraction experiments. The samples with the thickness smaller than 100 nm were characterized by optical microscopy, atomic force microscopy (AFM), and TEM (see details in Section S1, Supporting Information). The femtosecond electron diffraction experiments with three different samples and two FED systems (50 keV and 3 MeV FED) were repeated to ensure the reproducibility of the experiments and conclusions.

Structure Factor Calculation and Global Fit of the Structural Dynamics: The intensity of a Bragg reflection, $I \propto |F|^2$, at the time delay point Δt can be calculated by the structure factor:

$$F\ (hkl, \Delta t) = \sum_j T_j f_j \cdot \exp\left[-i2\pi\left(h\left(x_j + \Delta x_{j,\mathrm{diso}} + \Delta x_{j,\mathrm{disp}}\right)\right.\right.$$
$$\left.\left. + k\left(y_j + \Delta y_{j,\mathrm{diso}} + \Delta y_{j,\mathrm{disp}}\right) + l\left(z_j + \Delta z_{j,\mathrm{diso}} + \Delta z_{j,\mathrm{disp}}\right)\right)\right] \quad (1)$$

where the summation runs over all atoms in the supercell (one to a few unit cells) of the local structure, f_j is the atomic form factor for the jth atom, $r_j = x_j\,\hat{a} + y_j\hat{b} + z_j\hat{c}$ is the vector position of the atom in the supercell and (hkl) is the Miller indices. $\Delta x_{j,\mathrm{diso}}$, $\Delta y_{j,\mathrm{diso}}$, and $\Delta z_{j,\mathrm{diso}}$ are the displacements deviating from the ideal symmetry position, which indicates the static disorder at the ground state. $\Delta x_{j,\mathrm{disp}}$, $\Delta y_{j,\mathrm{disp}}$, and $\Delta z_{j,\mathrm{disp}}$ are the time-dependent displacements induced by ultrafast photoexcitation. T_j is the thermal vibration, i.e., the Debye-Waller effect, induced by ultrafast photoexcitation:

$$T_j = \exp(-M)\ ,\ M = 8\pi^2\left\langle \mu^2 \right\rangle (\sin\theta/\lambda)^2 \quad (2)$$

M denotes the Debye-Waller factor, θ is half the scattering angle, and $\langle \mu^2 \rangle$ represents the mean square displacement of atoms in the supercell. Therefore, the thermal vibration, the static local disorder, and the photoexcited displacement can be identified by Bragg reflections. To quantify these parameters, a global fit of the intensity changes overall experimental acquired Bragg reflections in the whole femtosecond to picosecond time scale was taken. The minimum standard error (SE) was searched between the calculated and the experimental intensity changes of the all (hkl) reflections by the least square method:

$$\mathrm{SE} = \sum_{hkl} \frac{\left(\Delta|F_{hkl}|^2 - \Delta I_{hkl\_\mathrm{exp}}\right)^2}{n * \Delta I_{hkl\_\mathrm{exp}}{}^2} \quad (3)$$

where $\Delta|F_{hkl}|^2$ is the calculated intensity change, $\Delta I_{hkl\_\mathrm{exp}}$ is the experimental intensity change of the (hkl) reflection, and n is the number of the associated reflections. To avoid reaching the local minimum instead of the global minimum, the search results with SE ≤ 0.3 and the convergence of the search results in this range are always checked. The upper limit of SE to 0.3 corresponded to a tolerance of ≈±50% of the experimental intensity changes, which was much higher than the intensity resolution of the FED systems. During the search, the amplitude boundary of both the static/photoexcited displacement and the thermal vibration was set to within the 15% of the bond length (the Lindemann criteria). The step size of all parameter changes in the search is dynamically adjusted to ensure the convergence of the search results as well as the calculation efficiency. Details on specific calculations are shown in Supporting Information. More discussion on the methodology of using Bragg reflections to quantify the local structure is shown in Section S11 in the Supporting Information.

TDDFT-MD and DFT Simulation: The TDDFT-MD calculations were performed in a time-dependent ab initio package. Numerical atomic orbitals with double zeta polarization were employed as the basis set. The plane-wave energy cutoff was set to 300 Ry. The Brillouin zone was sampled using a $3 \times 7 \times 7$ k-point mesh for the unit cell and the PBE-D3 method of Grimme with Becke-Jonson damping was applied. The Gaussian-type laser pulse utilized in the study was given by $E(t) = E_0 \cos(\omega t)\cdot\exp[-(t - t_0)^2 / 2\delta^2]$, where the maximum field intensity E_0 is 0.04 V Å^{-1}, and $t_0 = 100$ fs is the temporal location of the electric field peak. The laser pulse was linearly polarized along the y axis. The photon energy and FWHM were set

as 1.55 eV ($\lambda = 800$ nm) and 30 fs, respectively. The laser fluence was 0.17 mJ cm^{-2}. The time-dependent Kohn-Sham wave functions of the system evolve in a microcanonical ensemble (constant-volume ensemble) ensembled with a time step of 50 attoseconds.

The DFT calculations were performed based on Vienna ab initio simulation package. The exchange-correlation effect was described within the generalized gradient approximation in the Perdew–Burke–Ernzerhof (PBE) functional, together with the projector augmented wave potentials. A $1 \times 2 \times 2$ supercell was used with 1 Sn vacancy ($Sn_{15}Se_{16}$) in the simulation to verify the disordered structure of SnSe. The Brillouin zone was sampled using a $3 \times 5 \times 5$ *k*-point mesh for the supercell and the PBE-D3 method of Grimme with Becke-Jonson damping is applied. The plane-wave energy cutoff was set to 450 eV.

Supporting Information

Supporting Information is available from the Wiley Online Library or from the author.

Acknowledgements

The authors acknowledge Dr. Kunqi Xu and Prof. Zhiwen Shi from School of Physics and Astronomy, Shanghai Jiao Tong University for the characterization of the sample with AFM. This work was supported by the Shanghai Soft X-ray Free Electron Laser Facility. This work was supported by National Key R&D Program of China (No.2021YFA1400202), the National Natural Science Foundation of China (Nos. 11925505, 11974241, 12304024, 12025407, 11934003, and 12335010), the US-NSF Cooperative agreement (Grant numbers DMR-1644779 and DMR-2128556), and the state of Florida. [Correction added on March 22, 2024, after first online publication: Figures were changed.]

Conflict of Interest

The authors declare no conflict of interest.

Author Contributions

J.L. and Q.Y. contributed equally to this work. Y.Q. devised the project and conceived the presented ideas. Y.Q. and J.L. prepared and characterized the sample. J.L. and Y.Q. performed the keV and MeV femtosecond electron diffraction experiments with help from L.Y. and C.Y. Z.C. maintained the MeV-FED beamline under the supervision of D.X. Y.Q. and J.L. analyzed the experimental data and built up the model presented in the paper. Q.Y. performed the TDDFT-MD simulation under the supervision of S.M. Y.Q. and J.L. wrote the paper with contributions from all other authors. J.C., D.X., and S.M. supervised the project.

Data Availability Statement

The data that support the findings of this study are available from the corresponding author upon reasonable request.

Keywords

Einstein oscillator, femtosecond electron diffraction, local anharmonicity, local disorder, tin selenide

Received: December 15, 2023
Revised: February 22, 2024
Published online: March 12, 2024

[1] a) M. M. Yang, Z. D. Luo, Z. Mi, J. Zhao, E. Sharel Pei, M. Alexe, *Nature* **2020**, *584*, 377; b) J. G. Horstmann, H. Bockmann, B. Wit, F. Kurtz, G. Storeck, C. Ropers, *Nature* **2020**, *583*, 232; c) T. Senthil, *Annu. Rev. Condens. Matter Phys.* **2015**, *6*, 299; d) F. Tang, H. C. Po, A. Vishwanath, X. Wan, *Nature* **2019**, *566*, 486.

[2] A. Simonov, A. L. Goodwin, *Nat. Rev. Chem.* **2020**, *4*, 657.

[3] a) H. Pirie, E. Mascot, C. E. Matt, Y. Liu, P. Chen, M. H. Hamidian, S. Saha, X. Wang, J. Paglione, G. Luke, D. Goldhaber-Gordon, C. F. Hirjibehedin, J. C. S. Davis, D. K. Morr, J. E. Hoffman, *Science* **2023**, *379*, 1214; b) S. H. Skjærvø, Q. N. Meier, M. Feygenson, N. A. Spaldin, S. J. L. Billinge, E. S. Bozin, S. M. Selbach, *Phys. Rev. X* **2019**, *9*, 031001; c) E. Dagotto, *Science* **2005**, *309*, 257; d) E. S. Božin, C. D. Malliakas, P. Souvatzis, T. Proffen, N. A. Spaldin, M. G. Kanatzidis, S. J. L. Billinge, *Science* **2010**, *330*, 1660; e) G. J. Snyder, M. Christensen, E. Nishibori, T. Caillat, B. B. Iversen, *Nat. Mater.* **2004**, *3*, 458; f) Y. Qi, N. Chen, T. Vasileiadis, D. Zahn, H. Seiler, X. Li, R. Ernstorfer, *Phys. Rev. Lett.* **2022**, *129*, 135701; g) A. V. Kolobov, M. Krbal, P. Fons, J. Tominaga, T. Uruga, *Nat. Chem.* **2011**, *3*, 311; h) S. A. J. Kimber, J. Zhang, C. H. Liang, G. G. Guzman-Verri, P. B. Littlewood, Y. Cheng, D. L. Abernathy, J. M. Hudspeth, Z. Z. Luo, M. G. Kanatzidis, T. Chatterji, A. J. Ramirez-Cuesta, S. J. L. Billinge, *Nat. Mater.* **2023**, *22*, 311.

[4] a) S. J. L. Billinge, I. Levin, *Science* **2007**, *316*, 561; b) J. Shamblin, M. Feygenson, J. Neuefeind, C. L. Tracy, F. Zhang, S. Finkeldei, D. Bosbach, H. Zhou, R. C. Ewing, M. Lang, *Nat. Mater.* **2016**, *15*, 507; c) A. Bencan, E. Oveisi, S. Hashemizadeh, V. K. Veerapandiyan, T. Hoshina, T. Rojac, M. Deluca, G. Drazic, D. Damjanovic, *Nat. Commun.* **2021**, *12*, 3509; d) D. J. Voneshen, K. Refson, E. Borissenko, M. Krisch, A. Bosak, A. Piovano, E. Cemal, M. Enderle, M. J. Gutmann, M. Hoesch, M. Roger, L. Gannon, A. T. Boothroyd, S. Uthayakumar, D. G. Porter, J. P. Goff, *Nat. Mater.* **2013**, *12*, 1028.

[5] E. C. O'Quinn, K. E. Sickafus, R. C. Ewing, G. Baldinozzi, J. C. Neuefeind, M. G. Tucker, A. F. Fuentes, D. Drey, M. K. Lang, *Sci. Adv.* **2020**, *6*, eabc2758.

[6] a) Q. Yan, M. G. Kanatzidis, *Nat. Mater.* **2022**, *21*, 503; b) X. L. Shi, J. Zou, Z. G. Chen, *Chem. Rev.* **2020**, *120*, 7399.

[7] a) Y. Xiao, L.-D. Zhao, *Science* **2020**, *367*, 1196; b) L.-D. Zhao, S.-H. Lo, Y. Zhang, H. Sun, G. Tan, C. Uher, C. Wolverton, V. P. Dravid, M. G. Kanatzidis, *Nature* **2014**, *508*, 373; c) L.-D. Zhao, C. Chang, G. Tan, M. G. Kanatzidis, *Environ. Sci.* **2016**, *9*, 3044; d) D. Liu, D. Wang, T. Hong, Z. Wang, Y. Wang, Y. Qin, L. Su, T. Yang, X. Gao, Z. Ge, B. Qin, L.-D. Zhao, *Science* **2023**, *380*, 841.

[8] C. W. Li, J. Hong, A. F. May, D. Bansal, S. Chi, T. Hong, G. Ehlers, O. Delaire, *Nat. Phys.* **2015**, *11*, 1063.

[9] Y. Xiao, C. Chang, Y. Pei, D. Wu, K. Peng, X. Zhou, S. Gong, J. He, Y. Zhang, Z. Zeng, L.-D. Zhao, *Phys. Rev. B* **2016**, *94*, 125203.

[10] T. Lanigan-Atkins, S. Yang, J. L. Niedziela, D. Bansal, A. F. May, A. A. Puretzky, J. Y. Y. Lin, D. M. Pajerowski, T. Hong, S. Chi, G. Ehlers, O. Delaire, *Nat. Commun.* **2020**, *11*, 4430.

[11] a) M. Y. Hu, X. Yong, N. J. English, J. S. Tse, *Phys. Rev. B* **2021**, *104*, 184303; b) J. S. Kang, H. Wu, M. Li, Y. Hu, *Nano Lett.* **2019**, *19*, 4941.

[12] a) D. Wu, L. Wu, D. He, L.-D. Zhao, W. Li, M. Wu, M. Jin, J. Xu, J. Jiang, L. Huang, Y. Zhu, M. G. Kanatzidis, J. He, *Nano Energy* **2017**, *35*, 321; b) L.-D. Zhao, S.-H. Lo, Y. Zhang, H. Sun, G. Tan, C. Uher, C. Wolverton, V. P. Dravid, M. G. Kanatzidis, *Nature* **2016**, *539*, E2; c) P. C. Wei, S. Bhattacharya, J. He, S. Neeleshwar, R. Podila, Y. Y. Chen, A. M. Rao, *Nature* **2016**, *539*, E1; d) K. Sraitrova, J. Cizek, V. Holy, T. Plechacek, L. Benes, M. Jarosova, V. Kucek, C. Drasar, *Phys. Rev. B* **2019**, *99*, 035306; e) G. Duvjir, T. Min, T. T Ly, T. Kim, A.-T. Duong, S. Cho, S. H. Rhim, J. Lee, J. Kim, *Appl. Phys. Lett.* **2017**, *110*, 262106; f) M. Sist, J. Zhang, B. B Iversen, *Acta Crystallogr. B* **2016**, *72*, 310.

[13] a) S. Mukhopadhyay, D. S. Parker, B. C. Sales, A. A. Puretzky, M. A. McGuire, L. Lindsay, *Science* **2018**, *360*, 1455; b) M. Simoncelli, N. Marzari, F. Mauri, *Nat. Phys.* **2019**, *15*, 809.
[14] A. Hirata, P. Guan, T. Fujita, Y. Hirotsu, A. Inoue, A. R. Yavari, T. Sakurai, M. Chen, *Nat. Mater.* **2011**, *10*, 28.
[15] Y. Qi, M. Guan, D. Zahn, T. Vasileiadis, H. Seiler, Y. W. Windsor, H. Zhao, S. Meng, R. Ernstorfer, *ACS Nano* **2022**, *16*, 11124.
[16] a) B. Guzelturk, T. Winkler, T. W. J. Van de Goor, M. D. Smith, S. A. Bourelle, S. Feldmann, M. Trigo, S. W. Teitelbaum, H. G. Steinruck, G. A. de la Pena, R. Alonso-Mori, D. Zhu, T. Sato, H. I. Karunadasa, M. F. Toney, F. Deschler, A. M. Lindenberg, *Nat. Mater.* **2021**, *20*, 618; b) A. Zong, A. Kogar, Y.-Q. Bie, T. Rohwer, C. Lee, E. Baldini, E. Ergeçen, M. B. Yilmaz, B. Freelon, E. J. Sie, H. Zhou, J. Straquadine, P. Walmsley, P. E. Dolgirev, A. V. Rozhkov, I. R. Fisher, P. Jarillo-Herrero, B. V. Fine, N. Gedik, *Nat. Phys.* **2019**, *15*, 27.
[17] F. Qi, Z. Ma, L. Zhao, Y. Cheng, W. Jiang, C. Lu, T. Jiang, D. Qian, Z. Wang, W. Zhang, P. Zhu, X. Zou, W. Wan, D. Xiang, J. Zhang, *Phys. Rev. Lett.* **2020**, *124*, 134803.
[18] M. A. Krivoglaz, *X-Ray and Neutron Diffraction in Nonideal Crystals*, Springer, Berlin, Heidelberg **1996**.
[19] T. Konstantinova, L. Wu, M. Abeykoon, R. J. Koch, A. F. Wang, R. K. Li, X. Shen, J. Li, J. Tao, I. A. Zaliznyak, C. Petrovic, S. J. L. Billinge, X. J. Wang, E. S. Bozin, Y. Zhu, *Phys. Rev. B* **2019**, *99*, 180102(R).
[20] L. P. Rene de Cotret, M. R. Otto, J. H. Pohls, Z. Luo, M. G. Kanatzidis, B. J. Siwick, *Proc. Natl. Acad. Sci. U. S. A.* **2022**, *119*, e2113967119.
[21] a) L. Waldecker, R. Bertoni, H. Hubener, T. Brumme, T. Vasileiadis, D. Zahn, A. Rubio, R. Ernstorfer, *Phys. Rev. Lett.* **2017**, *119*, 036803; b) M. Harb, H. Enquist, A. Jurgilaitis, F. T. Tuyakova, A. N. Obraztsov, J. Larsson, *Phys. Rev. B* **2016**, *93*, 104104.
[22] a) M. Harb, W. Peng, G. Sciaini, C. T. Hebeisen, R. Ernstorfer, M. A. Eriksson, M. G. Lagally, S. G. Kruglik, R. J. D. Miller, *Phys. Rev. B* **2009**, *79*, 094301; b) I. González Vallejo, G. Gallé, B. Arnaud, S. A. Scott, M. G. Lagally, D. Boschetto, P.-E. Coulon, G. Rizza, F. Houdellier, D. Le Bolloc'h, J. Faure, *Phys. Rev. B* **2018**, *97*, 054302; c) H. Zhang, W. Li, J. Essman, C. Quarti, I. Metcalf, W.-Y. Chiang, S. Sidhik, J. Hou, A. Fehr, A. Attar, M.-F. Lin, A. Britz, X. Shen, S. Link, X. Wang, U. Bergmann, M. G. Kanatzidis, C. Katan, J. Even, J.-C. Blancon, A. D. Mohite, *Nat. Phys.* **2023**, *19*, 545.
[23] a) X.-L. Shi, W.-Y. Chen, X. Tao, J. Zou, Z.-G. Chen, *Mater. Horiz.* **2020**, *7*, 3065; b) Z. Wang, C. Fan, Z. Shen, C. Hua, Q. Hu, F. Sheng, Y. Lu, H. Fang, Z. Qiu, J. Lu, Z. Liu, W. Liu, Y. Huang, Z. A. Xu, D. W. Shen, Y. Zheng, *Nat. Commun.* **2018**, *9*, 47; c) J. Li, J. Li, K. Sun, L. Wu, R. Li, J. Yang, X. Shen, X. Wang, H. Luo, R. J. Cava, I. K. Robinson, X. Jin, W. Yin, Y. Zhu, J. Tao, *Phys. Rev. B* **2020**, *101*, 100304(R); d) M. Eichberger, H. Schafer, M. Krumova, M. Beyer, J. Demsar, H. Berger, G. Moriena, G. Sciaini, R. J. Miller, *Nature* **2010**, *468*, 799; e) V. R. Morrison, R. P. Chatelain, K. L. Tiwari, A. Hendaoui, A. Bruhács, M. Chaker, B. J. Siwick, *Science* **2014**, *346*, 445.
[24] a) S. Sadasivam, M. K. Y. Chan, P. Darancet, *Phys. Rev. Lett.* **2017**, *119*, 136602; b) R. P. Chatelain, V. R. Morrison, B. L. M. Klarenaar, B. J. Siwick, *Phys. Rev. Lett.* **2014**, *113*, 235502.
[25] a) Y. Huang, S. Yang, S. Teitelbaum, G. De la Peña, T. Sato, M. Chollet, D. Zhu, J. L. Niedziela, D. Bansal, A. F. May, A. M. Lindenberg, O. Delaire, D. A. Reis, M. Trigo, *Phys. Rev. X* **2022**, *12*, 011029; b) W. Wang, L. Wu, J. Li, N. Aryal, X. Jin, Y. Liu, M. Fedurin, M. Babzien, R. Kupfer, M. Palmer, C. Petrovic, W. Yin, M. P. M. Dean, I. K. Robinson, J. Tao, Y. Zhu, *npj Quantum Mater.* **2021**, *6*, 97.
[26] Y. Zhou, W. Zhang, E. Ma, V. L. Deringer, *Nat. Electron.* **2023**, *6*, 746.
[27] a) M. Xu, D.-L. Bao, A. Li, M. Gao, D. Meng, A. Li, S. Du, G. Su, S. J. Pennycook, S. T. Pantelides, W. Zhou, *Nat. Mater.* **2023**, *22*, 612; b) F. S. Hage, G. Radtke, D. M. Kepaptsoglou, M. Lazzeri, Q. M. Ramasse, *Science* **2020**, *367*, 1124.
[28] a) T. S. Grigera, V. Martín-Mayor, G. Parisi, P. Verrocchio, *Nature* **2003**, *422*, 289; b) H. Shintani, H. Tanaka, *Nat. Mater.* **2008**, *7*, 870.
[29] G. Sciaini, M. Harb, S. G. Kruglik, T. Payer, C. T. Hebeisen, F. J. zu Heringdorf, M. Yamaguchi, M. Horn-von Hoegen, R. Ernstorfer, R. J. Miller, *Nature* **2009**, *458*, 56.
[30] a) Y. Xia, K. Pal, J. He, V. Ozolins, C. Wolverton, *Phys. Rev. Lett.* **2020**, *124*, 065901; b) A. Jain, *Phys. Rev. B* **2020**, *102*, 201201(R); c) Z. Zeng, C. Zhang, Y. Xia, Z. Fan, C. Wolverton, Y. Chen, *Phys. Rev. B* **2021**, *103*, 224307.
[31] M. Okawa, Y. Akabane, M. Maeda, G. Tan, L.-D. Zhao, M. G. Kanatzidis, T. Suzuki, M. Watanabe, J. Xu, Q. Ren, M. Fujisawa, T. Kanai, J. Itatani, S. Shin, K. Okazaki, N. L. Saini, T. Mizokawa, *Scr. Mater.* **2023**, *223*, 115081.
[32] H. Xie, E. S. Bozin, Z. Li, M. Abeykoon, S. Banerjee, J. P. Male, G. J. Snyder, C. Wolverton, S. J. L. Billinge, M. G. Kanatzidis, *Adv. Mater.* **2022**, *34*, 2202255.